PHYSICAL REVIEW C **91**, 024606 (2015)

Low-energy ^{9}Be + ^{208}Pb scattering, breakup, and fusion within a four-body model

P. Descouvemont,[1,*] T. Druet,[1] L. F. Canto,[2,3] and M. S. Hussein[4,5,6]

[1]*Physique Nucléaire Théorique et Physique Mathématique, C.P. 229, Université Libre de Bruxelles (ULB), B 1050 Brussels, Belgium*
[2]*Instituto de Física, Universidade Federal do Rio de Janeiro, C.P. 68528, 21941-972 Rio de Janeiro, RJ, Brazil*
[3]*Instituto de Física, Universidade Federal Fluminense, Av. Gal. Milton Tavares de Souza s/n, Niterói, RJ, Brazil*
[4]*Departamento de Física Matemática, Instituto de Física, Universidade de São Paulo, C.P. 66318, 05314-970 São Paulo, SP, Brazil*
[5]*Instituto de Estudos Avançados, Universidade de São Paulo, C.P. 72012, 05508-970 São Paulo, SP, Brazil*
[6]*Departamento de Física, Instituto Tecnológico de Aeronáutica, CTA, São José dos Campos, São Paulo, SP, Brazil*

(Received 12 December 2014; published 11 February 2015)

We investigate ^{9}Be + ^{208}Pb elastic scattering, breakup, and fusion at energies around the Coulomb barrier. The three processes are described simultaneously, with identical conditions of calculations. The ^{9}Be nucleus is defined in an $\alpha + \alpha + n$ three-body model, using the hyperspherical coordinate method. We first analyze spectroscopic properties of ^{9}Be and show that the model provides a fairly good description of the low-lying states. The scattering with ^{208}Pb is then studied with the continuum discretized coupled channel method, where the $\alpha + \alpha + n$ continuum is approximated by a discrete number of pseudostates. The use of a three-body model for ^{9}Be improves previous theoretical works, where ^{9}Be is assumed to have a two-body structure (^{8}Be + n or ^{5}He + α), although neither ^{8}Be nor ^{5}He are bound. Optical potentials for the α + ^{208}Pb and n + ^{208}Pb systems are taken from the literature. We present cross sections at different energies, and we investigate the convergence with respect to the truncation of the $\alpha + \alpha + n$ continuum. In general, good agreement with experiment is obtained, despite no parameter fitting being made. We show that continuum effects increase at low energies, and we confirm that breakup channels enhance the fusion cross sections below the Coulomb barrier.

DOI: 10.1103/PhysRevC.91.024606 PACS number(s): 24.10.Eq, 25.70.Bc, 25.70.Jj

I. INTRODUCTION

Many experiments have been performed with the ^{9}Be nucleus, used as a target or as a projectile [1]. Although ^{9}Be is stable, it presents a Borromean structure, as the well-known halo nucleus ^{6}He. None of the two-body subsystems $\alpha + n$ or $\alpha + \alpha$ is bound in ^{9}Be, which has important consequences on the theoretical description of this nucleus. Precise wave functions must include the three-body nature of ^{9}Be. The hyperspherical formalism is an ideal tool to describe three-body Borromean systems, as it does not assume a specific two-body structure and considers the three particles $\alpha + \alpha + n$ on an equal footing. This model has been successfully applied to several exotic nuclei, such as ^{6}He [2] or ^{11}Li [3], and to more tightly bound nuclei such as ^{9}Be [4] or ^{12}C [5].

In the present work, we aim at investigating ^{9}Be scattering on a heavy target. The reaction framework is the continuum discretized coupled-channel (CDCC) method [6–8], which is well adapted to weakly bound projectiles since it allows one to include breakup channels. Originally, the CDCC method was developed to describe deuteron elastic scattering [6]. Owing to its low binding energy, deuteron breakup channels must be included, even in the calculation of the elastic cross sections.

Over the last decades, the CDCC method has been extended in various directions and in particular to reactions involving three-body projectiles such as ^{6}He [9] or ^{11}Li [10]. Going from two-body projectiles (such as $d = p + n$ or ^{7}Li $= \alpha + t$) to three-body projectiles strongly increases the complexity of the calculations, even if both options eventually end up with a standard coupled-channel system. The calculations are performed in three steps: (1) computing the ^{9}Be wave functions in the $\alpha + \alpha + n$ hyperspherical model; (2) evaluating the ^{9}Be + target potentials (including coupling terms) for all ^{9}Be states; (3) solving the coupled-channel system to provide the scattering matrices and eventually the cross sections. Calculations involved in each step are significantly more complicated for three-body projectiles than for two-body projectiles.

Many data have been obtained for ^{9}Be + ^{208}Pb elastic scattering [11,12], breakup [13,14], and fusion [15,16]. These experimental data provide a good opportunity to test ^{9}Be wave functions. Previous CDCC calculations, using a two-body approximation for ^{9}Be, show that breakup effects are important [12,17,18]. In a two-body model, ^{9}Be is assumed to have a ^{8}Be + n or ^{5}He + α cluster structure. This approximation presents several shortcomings: (i) ^{8}Be and ^{5}He are unbound, and assuming a pointlike structure is questionable; (ii) in a more rigorous three-body approach, both configurations are strictly equivalent, and the relative importance of the ^{8}Be + n and ^{5}He + α channels is not relevant; (iii) a two-body model of ^{9}Be requires ^{8}Be + ^{208}Pb or ^{5}He + ^{208}Pb optical potentials, which are not available. These different issues are more precisely addressed in a three-body model of ^{9}Be. No assumption should be made about the cluster structure, and α + ^{208}Pb as well as n + ^{208}Pb optical potentials are available in the literature.

Calculations of fusion cross sections deserve special attention. The fusion process provides strong tests of scattering models and has been investigated by many authors (see, for example, Refs. [19–21]). An important issue is associated with the concept of complete and incomplete fusion, according

*pdesc@ulb.ac.be

to whether the whole projectile fuses or just one of its fragments. For weakly bound nuclei, a recent coupled-channel calculation [22] suggests that the total fusion cross section is strongly suppressed at low energies, compared to model predictions. Our goal here is not to provide a deep analysis of the fusion cross section but to investigate this mechanism in conditions identical to those of elastic scattering. In most calculations, these processes are studied independently, with optical potentials optimized for each reaction.

The paper is organized as follows. In Sec. II, we briefly present the three-body model and apply it to spectroscopic properties of ^{9}Be. Section III provides an outline of the CDCC method with three-body projectiles. Using the ^{9}Be wave functions, we apply the CDCC formalism to the $^9\mathrm{Be} + {}^{208}\mathrm{Pb}$ system in Sec. IV. Elastic-scattering, breakup, and fusion cross sections are calculated at energies close to the Coulomb barrier. Conclusions and outlook are presented in Sec. V.

II. THREE-BODY MODEL OF ^{9}Be

A. Hyperspherical formalism

We present here the main properties of the hyperspherical method. Further detail can be found in Refs. [2,23,24]. For a three-body system, the Hamiltonian is given by

$$H_0 = \sum_{i=1}^{3} \frac{\boldsymbol{p}_i^2}{2m_i} + \sum_{i<j=1}^{3} V_{ij}(\boldsymbol{r}_i - \boldsymbol{r}_j), \tag{1}$$

where $\boldsymbol{r}_i$ and $\boldsymbol{p}_i$ are the space and momentum coordinates, respectively, of the three particles, and V_{ij} is the potential between nuclei i and j. We define scaled Jacobi coordinates as

$$\begin{aligned} \boldsymbol{x} &= \sqrt{\mu_{\alpha-\alpha}}(\boldsymbol{r}_3 - \boldsymbol{r}_2), \\ \boldsymbol{y} &= \sqrt{\mu_{Be-n}}\left(\boldsymbol{r}_1 - \frac{\boldsymbol{r}_2 + \boldsymbol{r}_3}{2}\right), \end{aligned} \tag{2}$$

where $\mu_{\alpha-\alpha} = 2$ and $\mu_{Be-n} = 8/9$. We assume that particle 1 is the neutron and particles 2 and 3 correspond to the α particles. Of course any other choice is possible, but the present set of coordinates allows us to account for the symmetry of the $\alpha + \alpha$ system and to reduce the number of components in the wave functions.

From coordinates (2), we define the hyperradius ρ and hyperangle α as

$$\begin{aligned} \rho^2 &= \boldsymbol{x}^2 + \boldsymbol{y}^2, \\ \alpha &= \arctan(y/x). \end{aligned} \tag{3}$$

For a given angular momentum j and parity π, a solution of the Schrödinger equation associated with (1) is expanded as

$$\begin{aligned} \Psi^{jm\pi} &= \sum_{l_x l_y l S} \Psi^{jm\pi}_{l_x l_y l S} \\ &= \rho^{-5/2} \sum_{\gamma K} \chi^{j\pi}_{\gamma K}(\rho)\, \mathcal{Y}^{jm}_{\gamma K}(\Omega_x, \Omega_y, \alpha), \end{aligned} \tag{4}$$

where K is the hypermomentum, typical of many-body systems [23,24]. In practice, the summation over K is truncated at a maximum value $K_{\max}$. In (4), $\gamma = (l_x, l_y, l, S)$ represents a set of quantum numbers, where l_x and l_y are the orbital momenta associated with $\boldsymbol{x}$ and $\boldsymbol{y}$, l is the total angular momentum, and S is the total intrinsic spin ($S = 1/2$ in the $\alpha + \alpha + n$ system). Functions $\mathcal{Y}^{jm}_{\gamma K}$ are hyperspherical harmonics and depend on five angles. These are well-known analytical functions [23,24]. Notice that, for a given K, the summation over γ is limited by the selection rules

$$\begin{aligned} K &= l_x + l_y + 2n, \\ |l_x - l_y| &\leqslant l \leqslant l_x + l_y, \\ |l - S| &\leqslant j \leqslant l + S, \end{aligned} \tag{5}$$

where n is a positive integer number. The number of γ values rapidly increases with K.

The hyperradial wave functions $\chi^{j\pi}_{\gamma K}(\rho)$ are obtained from a coupled-channel differential system [2]

$$\begin{aligned} &\left[-\frac{\hbar^2}{2m_N}\left(\frac{d^2}{d\rho^2} - \frac{(K+3/2)(K+5/2)}{\rho^2}\right) - E\right]\chi^{j\pi}_{\gamma K}(\rho) \\ &\quad + \sum_{K'\gamma'} V^{j\pi}_{K'\gamma',K\gamma}(\rho)\, \chi^{j\pi}_{\gamma' K'}(\rho) = 0, \end{aligned} \tag{6}$$

where m_N is the nucleon mass, and where $V^{j\pi}_{K'\gamma',K\gamma}(\rho)$ represents a matrix element of the potential term $V_{12} + V_{13} + V_{23}$ between hyperspherical harmonics. This system is solved here by using the Lagrange mesh method [5,25]. Each component of the hyperradial wave function is expanded as

$$\chi^{j\pi}_{\gamma K}(\rho) = \sum_{i=1}^{N_0} c^{j\pi}_{\gamma K i} u_i(\rho), \tag{7}$$

where $u_i(\rho)$ are Lagrange functions [5]. System (6) is therefore replaced by a standard eigenvalue problem. Typical values for N_0 are $N_0 \sim 20$–30.

The main advantage of Lagrange functions is that matrix elements are very simple if one uses the Gauss approximation corresponding to the mesh. For an operator $O(\rho)$ depending on the hyperradius only, a matrix element is given by

$$\langle \chi^{j\pi}_{\gamma K} | O | \chi^{j\pi}_{\gamma' K'} \rangle = \sum_{i=1}^{N_0} c^{j\pi}_{\gamma K i} c^{j\pi}_{\gamma' K' i} O(\rho_i), \tag{8}$$

where $O(\rho_i)$ is the operator defined at the mesh points ρ_i. This means that no integral is needed for the matrix elements (see Ref. [25] for more detail).

B. Application to the $\alpha + \alpha + n$ system

The determination of the ^{9}Be wave functions is the first step for the $^9\mathrm{Be} + {}^{208}\mathrm{Pb}$ CDCC calculation. The spectroscopy of ^{9}Be in cluster models has been performed in previous microscopic [26–28] and nonmicroscopic [4,29–31] models. Here we briefly describe the specificities of our approach. An important issue is the role of $^8\mathrm{Be}^\star + n$ configurations, which were predicted to be important in low-lying states [26]. This was subsequently supported by experimental data on the ^{9}Be breakup [32]. Most calculations assume $^8\mathrm{Be} + n$ and/or $^5\mathrm{He} + \alpha$ configurations (see, for example, Ref. [12]). From

the theoretical point of view these two configurations are strictly equivalent provided that the basis is large enough. Our choice (2) of the Jacobi coordinates assumes a ^{8}Be + n structure, but the ^{5}He + α configuration is obtained by a unitary transform, using the Raynal-Revai coefficients [23].

For the $\alpha + \alpha$ interaction, we use the deep potential of Buck *et al.* [33]. The $\alpha + n$ interaction is taken from Kanada *et al.* [34]. Both (real) potentials accurately reproduce the $\alpha + \alpha$ and α + nucleon phase shifts in a wide energy range. These deep potentials contain additional bound states, which aim at simulating the Pauli forbidden states. Additional deep states are removed in the three-body calculation by using a supersymmetric transform [35].

With these potentials, the ^{9}Be ground state is too bound (−3.12 MeV, while the experimental value is −1.57 MeV with respect to the $\alpha + \alpha + n$ threshold). We have therefore introduced a phenomenological three-body force as

$$V_{3B}(\rho) = \frac{V_0}{1 + (\rho/\rho_0)^2}\delta_{KK'}\delta_{\gamma\gamma'}, \tag{9}$$

where $\rho_0 = 6$ fm [36]. Using $V_0 = 2.7$ MeV provides the experimental binding energy of the $3/2^-$ ground state. The wave functions (4) are determined with a Gauss-Laguerre mesh with $N_0 = 20$ and a scaling parameter $h = 0.3$ fm (see [5] for detail). Several tests have been performed to check the stability of the results with respect to these parameters. The truncation hypermoment is $K_{\max} = 20$. For $j^\pi = 3/2^-$, this choice leads to 100 values of (γK) in the system (6). This number is 135 for $j^\pi = 5/2^-$.

In Fig. 1, we show the convergence of the $3/2^-$ ground-state and $5/2^-$ energies as a function of $K_{\max}$. For negative-parity states, only odd K values are allowed. The $5/2^-$ state is a narrow resonance ($\Gamma = 0.78$ keV) and can be accurately described in a bound-state approximation. Figure 1 shows that a reasonable convergence is reached for $K_{\max} = 15$. The theoretical $5/2^-$ energy (0.67 MeV) is slightly too low compared to experiment (0.86 MeV), but no fit has been performed.

Spectroscopic properties of the $3/2^-$ and $5/2^-$ states are given in Table I. The quadrupole and magnetic moments (Q and μ, respectively), as well as the $E2$ transition probability, are in fair agreement with experiment, despite that no effective charge being used. The r.m.s matter radius (with a radius of 1.4 fm assumed for the α particle) is slightly smaller than the experimental interaction radius [37].

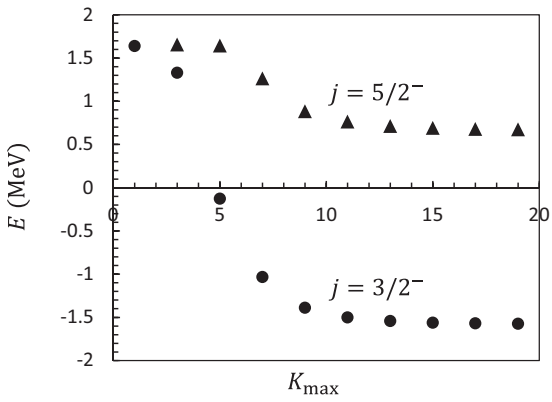

FIG. 1. Convergence of the $3/2^-$ and $5/2^-$ ^{9}Be energies as a function of the maximum hypermoment $K_{\max}$. Energies are defined from the $\alpha + \alpha + n$ threshold.

TABLE I. Spectroscopic properties of ^{9}Be.

	Theory	Experiment [38]
$Q(3/2^-)$ (e fm^2)	4.96	5.29 ± 0.04
$\mu(3/2^-)$ (μ_N)	−1.13	−1.18
$B(E2, 5/2^- \to 3/2^-)$ (W.u.)	20.1	24.4 ± 1.8
$\sqrt{r^2}$ (fm)	2.36	2.45 ± 0.01[a]

[a]Interaction radius.

The wave functions are analyzed in Table II. The ^{8}Be components are deduced from the amplitudes in the l_x partial waves as

$$C^{j\pi}_{l_x} = \sum_{l_y,l,S} \left|\left\langle \Psi^{j\pi}_{l_x l_y l S} \middle| \Psi^{j\pi}_{l_x l_y l S} \right\rangle\right|^2, \tag{10}$$

where $l_x = 0$ corresponds to the ^{8}Be ground state and $l_x = 2$ to the 2^+ excited state. Table II confirms previous microscopic studies [26] and experimental data [14,32], which suggest that the 2^+ component is important. In particular, Brown *et al.* [14] observe a branching ratio for the $5/2^-$ decay to the $n + {}^8\mathrm{Be}(2^+)$ channel of $94 \pm 2\%$, which is remarkably close to the 2^+ amplitude found here (95.0%).

Table II also presents the l contributions $C^{j\pi}_l$ in the wave functions; they are obtained as in (10) by summing over l_x in place of l. Each j^π contains two l values ($l = j \pm 1/2$). From Table II, we deduce that the lowest value is strongly dominant.

The $3/2^-$ wave function is shown in Fig. 2, in terms of the probability function $P^{j\pi}(x,y)$ defined as

$$P^{j\pi}(x,y) = \int d\Omega_x d\Omega_y |\Psi^{jm\pi}(\boldsymbol{x},\boldsymbol{y})|^2 \tag{11}$$

and is plotted as a function of the relative coordinates $r_{\alpha\text{-}\alpha} = x/\sqrt{2}$ and $r_{Be\text{-}n} = y\sqrt{9/8}$. The normalization is such that

$$\int P^{j\pi}(r_{\alpha-\alpha}, r_{Be-n}) dr_{\alpha-\alpha} dr_{Be-n} = 1. \tag{12}$$

Figure 2 presents a maximum near $r_{\alpha\text{-}\alpha} \approx 3$ fm and $r_{Be\text{-}n} \approx 2.2$ fm. The α-α distance is similar to the value found in the

TABLE II. Components (in %) $C^{j\pi}_{l_x}$ (10) and $C^{j\pi}_l$ (see text) of the $3/2^-$ and $5/2^-$ states.

$C^{j\pi}_{l_x}$	$j = 3/2^-$	$j = 5/2^-$
^{8}Be(0^+)	50.6	0.4
^{8}Be(2^+)	48.4	95.0
^{8}Be(4^+)	1.0	4.5
$C^{j\pi}_l$		
$l = 1$	84.8	–
$l = 2$	15.2	93.8
$l = 3$	–	6.2

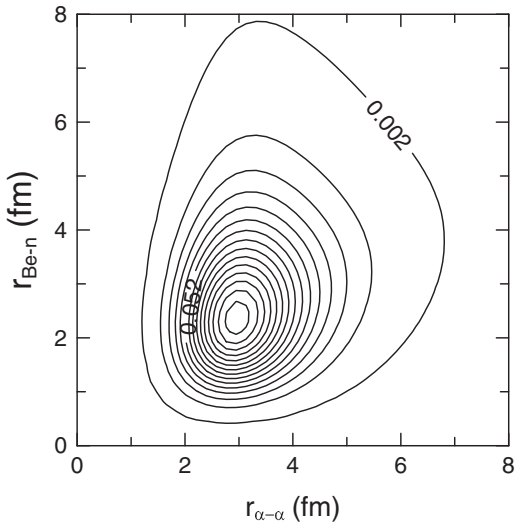

FIG. 2. Probability function (11) of the ^{9}Be ground state. The curves are drawn in steps of 0.005.

ground state of ^{12}C [5]. It is also consistent with a microscopic cluster calculation [39], where the optimal α-α distance was found close to 3 fm.

III. THE CDCC METHOD

A. Outline

We present here a brief outline of the CDCC method [7], and we refer to Ref. [40] for specificities of three-body projectiles. The CDCC method is based on approximate solutions of the projectile Hamiltonian (1)

$$H_0\Psi_k^{jm\pi} = E_{0,k}^{j\pi}\Psi_k^{jm\pi}, \tag{13}$$

where k are the excitation levels in partial wave $j\pi$. Solutions with $E_{0,k}^{j\pi} < 0$ correspond to bound states of the projectile, whereas $E_{0,k}^{j\pi} > 0$ correspond to narrow resonances or to approximations of the three-body continuum. These states cannot be associated with physical states and are referred to as pseudostates. As in most calculations, the target is assumed to remain in its ground state.

The Hamiltonian of the projectile + target system is written as

$$H(\boldsymbol{R},\boldsymbol{x},\boldsymbol{y}) = H_0(\boldsymbol{x},\boldsymbol{y}) - \frac{\hbar^2}{2\mu_{PT}}\Delta_{\boldsymbol{R}} + V(\boldsymbol{R},\boldsymbol{x},\boldsymbol{y}), \tag{14}$$

where μ_{PT} is the reduced mass of the system, and $\boldsymbol{R}$ is the relative coordinate (see Fig. 3). The potential term reads

$$V(\boldsymbol{R},\boldsymbol{x},\boldsymbol{y}) = V_{1t}(\boldsymbol{R},\boldsymbol{y}) + V_{2t}(\boldsymbol{R},\boldsymbol{x},\boldsymbol{y}) + V_{3t}(\boldsymbol{R},\boldsymbol{x},\boldsymbol{y}), \tag{15}$$

where the three components V_{it} are optical potentials between fragment i and the target. Owing to the present choice of the Jacobi coordinates (2), the potential between particle 1 (the neutron for ^{9}Be) does not depend on coordinate $\boldsymbol{x}$ or, equivalently, on $\boldsymbol{r}_{\alpha-\alpha}$ (see Fig. 3).

In order to solve the Schrödinger equation associated with (14), the total wave function with angular momentum

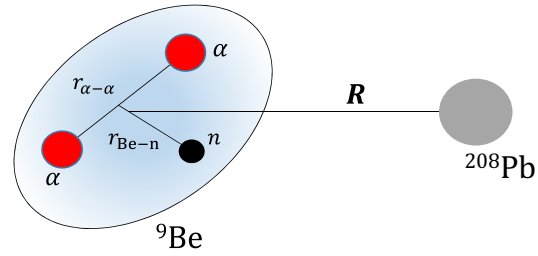

FIG. 3. (Color online) Coordinates involved in the present four-body model.

J and parity Π [$\Pi = \pi(-1)^L$] is expanded as

$$\Psi^{JM\Pi}(\boldsymbol{R},\boldsymbol{x},\boldsymbol{y}) = \sum_{j\pi kL} \varphi_{j\pi kL}^{JM\Pi}(\Omega_R,\boldsymbol{x},\boldsymbol{y}) g_{j\pi kL}^{J\Pi}(R), \tag{16}$$

where the channel wave functions are given by

$$\varphi_{j\pi kL}^{JM\Pi}(\Omega_R,\boldsymbol{x},\boldsymbol{y}) = i^L\left[\Psi_k^{j\pi}(\boldsymbol{x},\boldsymbol{y}) \otimes Y_L(\Omega_R)\right]^{JM}. \tag{17}$$

The sums over k and j are truncated at a maximum energy $E_{\max}$ and at a maximum angular momentum $j_{\max}$, respectively.

The radial functions $g_c^{J\pi}(R)$ [where we use the notation $c = (j,\pi,k,L)$] are obtained from the coupled-channel system

$$\left[-\frac{\hbar^2}{2\mu_{PT}}\left(\frac{d^2}{dR^2} - \frac{L(L+1)}{R^2}\right) + E_c - E\right] g_c^{J\Pi}(R) + \sum_{c'} V_{c,c'}^{J\Pi}(R) g_{c'}^{J\Pi}(R) = 0, \tag{18}$$

where E is the c.m. energy, E_c are the threshold energies, and the coupling potentials are given by matrix elements

$$V_{c,c'}^{J\Pi}(R) = \left\langle \varphi_c^{JM\Pi} \middle| V \middle| \varphi_{c'}^{JM\Pi} \right\rangle. \tag{19}$$

The integration is performed over Ω_R and over the internal coordinates $\boldsymbol{x}$ and $\boldsymbol{y}$. The calculation of these coupling potentials is much more complicated for three-body projectiles than for two-body projectiles. Out of the three potentials V_{it} in (15), matrix elements of V_{1t} are the easiest since V_{1t} does not depend on $\boldsymbol{x}$. The calculations of the two remaining terms V_{2t} and V_{3t} are performed by using the Raynal-Revai coefficients (see Refs. [40,41] for detail).

B. Scattering matrices

System (18) must be solved for positive scattering energies E ($E_c = 0$ corresponds to the ground state of the projectile). At large distances, the radial functions for open channels ($E > E_c$) tend to a combination of the incoming (I_c) and outgoing (O_c) Coulomb functions as

$$g_{c(\omega)}^{J\Pi}(R) \to I_c(k_cR)\delta_{c\omega} - U_{c\omega}^{J\Pi} O_c(k_cR), \tag{20}$$

where ω is the entrance channel, k_c is the wave number in channel c, and $U_{c\omega}^{J\Pi}$ is the scattering matrix. For closed channels ($E < E_c$), the radial functions tend to

$$g_{c(\omega)}^{J\Pi}(R) \to A_{c(\omega)}^{J\Pi} W_{-\eta_c,L+1/2}(2k_cR), \tag{21}$$

where η_c is the Sommerfeld parameter in channel c, $A_{c(\omega)}^{J\Pi}$ is the amplitude, and $W_{-\eta_c,L+1/2}(x)$ is the Whittaker function.

Elastic, inelastic, and breakup cross sections are then derived from the scattering matrices [42].

In the present work, we solve Eq. (18) with R-matrix theory [43], which is based on the existence of two regions. They are separated by the channel radius a: $R \leqslant a$, where the nuclear part in the interaction is important, and $R > a$, where only the Coulomb interaction remains and where the radial wave functions have reached their asymptotic form (20). In the internal region, the radial wave functions are expanded over a basis as

$$g_c^{J\Pi}(R) = \sum_{i=1}^{N} f_{ci}^{J\Pi} u_i(R), \tag{22}$$

and matrix elements

$$V_{ci,c'i'}^{J\Pi} = \int u_i^*(R) V_{c,c'}^{J\Pi}(R) u_{i'}(R)\, dR \tag{23}$$

are needed to compute the scattering matrix. As basis functions $u_i(R)$, we use here Lagrange functions based on Legendre polynomials [25,43]. Matrix elements (23) can be therefore computed without any integral over the relative coordinate R.

As mentioned before, a specificity of three-body projectiles is that matrix elements (19) are rather complicated and that three-body wave functions are of course required. Another specificity comes from the high level densities in the projectile. As three-body wave functions (4) contain many components (typically 100–200 for realistic values of $K_{\max}$), the Schrödinger equation associated with the projectile (13) provides many eigenvalues. The three-body continuum is therefore approximated by a large number of square-integrable wave functions. Examples for ^{6}He($=\alpha+n+n$) are given in [40]; they show that the level densities are much higher than for two-body projectiles. As a consequence, the coupled-channel system (18) involves a large number of equations.

C. Breakup cross sections

In the CDCC formalism, the continuum is simulated by a discrete number of square-integrable pseudostates. The cross section for "inelastic scattering" from the ground state to a pseudostate i is given by

$$\sigma_i(E) = \frac{\pi}{k^2} \sum_{J\Pi} \sum_{LL'} \frac{2J+1}{(2I_1+1)(2I_2+1)} \left|U_{\omega L,iL'}^{J\Pi}\right|^2, \tag{24}$$

where I_1 and I_2 are the spins of the colliding nuclei, ω is the ^{9}Be(g.s.) + ^{208}Pb entrance channel, and nondiagonal elements of the scattering matrix are involved [42]. In this definition, L and L' correspond to the angular momenta in the entrance and exit channels, respectively. Of course, a specific cross section to a single pseudostate does not have a physical meaning. However, the total breakup cross section can be approximated by the contribution of all pseudostates as

$$\sigma_{BU}(E) = \sum_i \sigma_i(E). \tag{25}$$

D. Fusion cross sections

The total fusion cross section σ_{TF} is defined from [20,21,42]

$$\sigma_{TF}(E) = \frac{\pi}{k^2} \sum_{J\Pi} (2J+1) T_F^{J\Pi}(E), \tag{26}$$

where k is the wave number and $T_F^{J\Pi}$ is the transmission coefficient for fusion in partial wave $J\Pi$. It can be obtained from the scattering matrices as

$$T_F^{J\Pi}(E) = \frac{1}{(2I_1+1)(2I_2+1)} \times \sum_{L_\omega, L} \left(\delta_{L_\omega L} - \left|U_{\omega L_\omega,\omega L}^{J\Pi}(E)\right|^2\right). \tag{27}$$

The reaction cross section can be defined in a similar way as

$$\sigma_R(E) = \frac{\pi}{k^2} \sum_{J\Pi} (2J+1) T_R^{J\Pi}(E), \tag{28}$$

with

$$T_R^{J\Pi}(E) = \frac{1}{(2I_1+1)(2I_2+1)} \times \sum_{L_\omega, L, i} \left(\delta_{L_\omega L}\delta_{\omega i} - \left|U_{\omega L_\omega, iL}^{J\Pi}(E)\right|^2\right). \tag{29}$$

With these definitions, the fusion cross section is related to the reaction and breakup cross sections by

$$\sigma_{TF}(E) = \sigma_R(E) - \sigma_{BU}(E). \tag{30}$$

Using flux conservation properties, the fusion transmission coefficient can be expressed from the imaginary part $W_{c,c'}^{J\Pi}(R)$ of the coupling potentials [42]. It is therefore strictly equivalent to

$$T_F^{J\Pi}(E) = -\frac{4k}{E} \frac{1}{(2I_1+1)(2I_2+1)} \sum_{L_\omega} \sum_{\alpha,\alpha',L,L'} \int g_{\omega L_\omega,\alpha L}^{J\Pi}(R) \times W_{\alpha L,\alpha' L'}^{J\Pi}(R)\, g_{\omega L_\omega,\alpha' L'}^{J\Pi}(R)\, dR, \tag{31}$$

where index α stands for $\alpha = (j,\pi,k)$; i.e., it does not depend on the angular momentum L [in other words $c = (\alpha, L)$]. In practice, using this definition is more complicated than (27) since it requires the wave functions, but it provides better accuracy at low energies, where the scattering matrix is close to unity. It also gives an approximate method to distinguish between complete and incomplete fusion [19]. Finally, it allows us to adapt the calculation to the experimental conditions of the fusion measurements. In the present case, fusion is experimentally defined as the capture of the whole charge of the projectile, where the neutron is not absorbed by the target. This can be addressed by removing the neutron-target potential in Eq. (32).

IV. APPLICATION TO THE ^{9}Be + ^{208}Pb SYSTEM

A. Conditions of the calculation

The four-body Hamiltonian (14) relies on α-^{208}Pb and n −^{208} Pb optical potentials. For α-^{208}Pb, we use the potential of Goldring *et al.* [44], which fits elastic cross sections in the range E_α = 14–23 MeV. The n −^{208} Pb optical potential is

taken from Ref. [45] at a neutron energy $E_n = E_{\rm lab}/9$ (where $E_{\rm lab}$ is the ^{9}Be energy).

The coupled-channel system (18) is solved with R-matrix theory [43]. In the coupling potentials (23), all multipoles are taken into account. In particular, the $E1$ mechanisms are expected to be important with highly charged targets. We use a channel radius $a = 30$ fm, where the nuclear components, as well as nonmonopole Coulomb terms, are small. At $R = 30$ fm, The Coulomb monopole potential is 15.74 MeV, whereas the coupling with the first $1/2^+$ pseudostate is 0.026 MeV (a term that decreases as $\sim 1/R^2$). Several tests have been performed to check the stability of the cross sections against variations of the channel radius. In the cross sections, we include partial waves up to $J_{\rm max} = 301/2$, which corresponds to $L_{\rm max} = 150$. This ensures precise convergence, even at backward angles.

The full calculations are performed with ^{9}Be partial waves $j^\pi = 1/2^\pm$, $3/2^\pm$,and $5/2^\pm$, and we use a truncation energy $E_{\rm max} = 12.5$ MeV. The ^{9}Be hyperradial wave functions are expanded over a Lagrange basis with $N_0 = 20$ [see Eq. (7)]. Using larger values does not affect the spectroscopic properties of the low-lying states. Of course, the discrete continuum spectrum is modified. The convergence against these parameters (j values, $E_{\rm max}$, and N_0) will be illustrated in the next section. The ^{9}Be pseudostates are shown in Fig. 4 for the most important angular momenta $j^\pi = 3/2^-$, $5/2^-$, and $1/2^+$. For these values, the ^{9}Be spectrum presents a bound state or a resonance. As expected, the level density is quite large. With a truncation energy of 12.5 MeV, the numbers of pseudostates are 36, 37, 59, 63, and 71 for $j^\pi = 1/2^+$, $1/2^-$, $3/2^+$, $3/2^-$, and $5/2^\pm$, respectively.

B. Elastic scattering

We first analyze the convergence of the elastic cross sections against the truncation parameters $E_{\rm max}$ and $j_{\rm max}$. This analysis is performed at two typical incident energies ($E_{\rm lab} = 38$ MeV, which approximately corresponds to the Coulomb barrier, and $E_{\rm lab} = 50$ MeV, above the Coulomb barrier), as convergence issues are known to depend on energy [46].

Figure 5 illustrates the convergence with the maximum pseudostate energy $E_{\rm max}$, which varies form 2.5 to 12.5 MeV (with partial waves $j^\pi = 1/2^\pm$, $3/2^\pm$, and $5/2^\pm$ being included). At $E_{\rm lab} = 50$ MeV, the convergence is reasonably fast, and pseudostates up to $E_{\rm max} = 10$ MeV are sufficient. The strongest sensitivity is obtained near $\theta \approx 60^\circ$. The convergence is slower at low energies, which confirms previous studies on ^{11}Be scattering [46,47]

In Fig. 6, we show the convergence with respect to the ^{9}Be partial waves j^π. The effect of breakup channels is obvious at both energies. For $E_{\rm max}$, a high accuracy requires several angular momenta, and the convergence is faster at high energies. This result emphasizes the numerical issues associated with CDCC calculations. The need of several partial waves in the projectile wave functions is very challenging for three-body projectiles, where the level density is rather large.

Figure 7 shows a comparison of theoretical and experimental ^{9}Be + ^{208}Pb elastic cross sections at various energies (with data taken from Refs. [11,48]). In contrast with optical-model calculations [11], no renormalization of the potential is needed. The absorption is simulated by the imaginary parts of the α-^{208}Pb and n –^{208} Pb interactions and by the $\alpha + \alpha + n$ discretized continuum.

The results of Fig. 7 confirm that continuum couplings are important. The single-channel calculation, limited to the ^{9}Be ground state (dashed lines), is significantly different from the data in the whole angular range. At backward angles, the

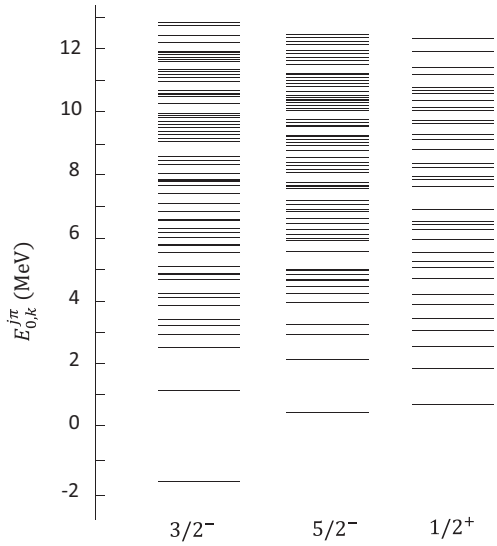

FIG. 4. Pseudostate energies $E^{j\pi}_{0,k}$ of ^{9}Be for different angular momenta j^π [see Eq. (13)] and for $N_0 = 20$. Energies are defined from the $\alpha + \alpha + n$ threshold.

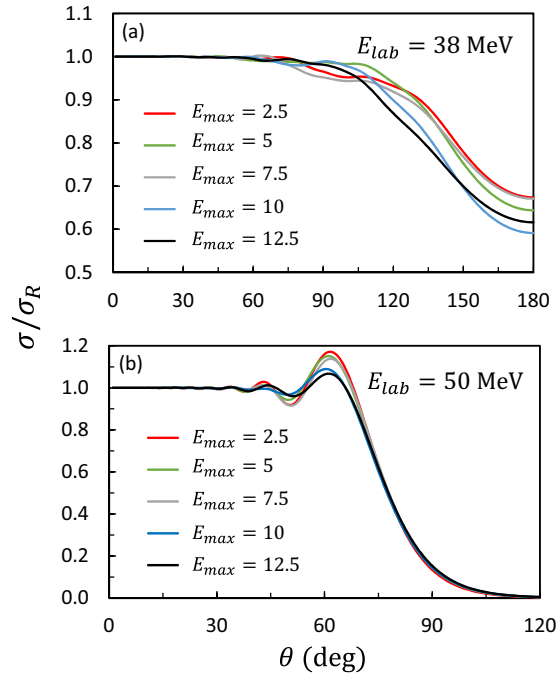

FIG. 5. (Color online) Influence of the truncation energy $E_{\rm max}$ at $E_{\rm lab} = 38$ MeV (upper panel) and $E_{\rm lab} = 50$ MeV (lower panel). The cross sections are divided by the Rutherford cross sections.

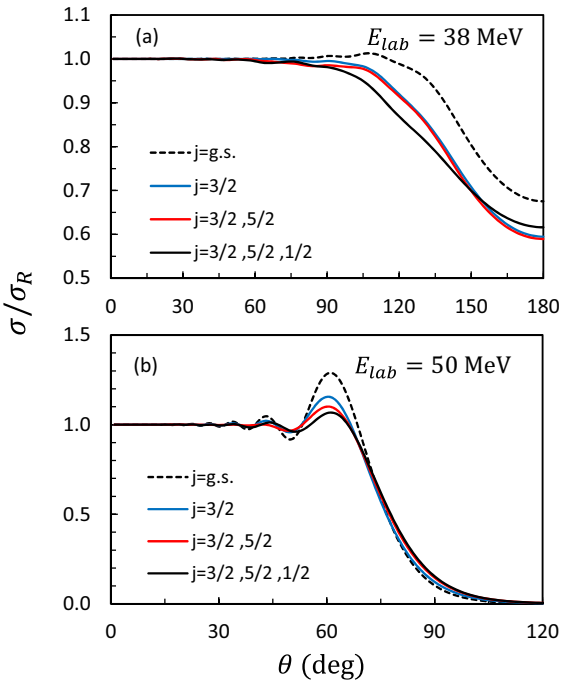

FIG. 6. (Color online) Influence of the ^{9}Be partial waves j^{π} at $E_{\rm lab}$ = 38 MeV (upper panel) and $E_{\rm lab}$ = 50 MeV (lower panel). The cross sections are divided by the Rutherford cross sections.

elastic cross sections are small and differences do not show up on a linear scale. However, the insets of Fig. 7, presented on a logarithmic scale, clearly confirm the role of breakup channels, even at large angles.

C. ^{9}Be breakup on a ^{208}Pb target

The investigation of breakup cross sections provides a strong constraint on CDCC calculations which, in contrast with the optical model-distorted-wave Born approximation, explicitly include the coupling to the ^{9}Be continuum states to all orders. As ^{9}Be is a Borromean nucleus, an $\alpha + \alpha + n$ description is quite appropriate to describe the continuum.

The CDCC breakup cross section is compared to the data of Woolliscroft *et al.* [13] in Fig. 8. For the elastic scattering, we consider various conditions of calculations. Let us first discuss the convergence against the truncation energy $E_{\rm max}$ (upper panel). Partial waves $j^{\pi} = 1/2^{\pm}$, $3/2^{\pm}$, and $5/2^{\pm}$ are included. Near the highest experimental energy, the cross sections are large, and the effect of $E_{\rm max}$ is relatively small. This effect, however, becomes more important at low energies. Using a low truncation energy $E_{\rm max}$ = 2.5 MeV provides 50% overestimation. Convergence effects against the ^{9}Be partial waves (lower panel) are even stronger. Calculations limited to $j^{\pi} = 3/2^{\pm}$, even with a high truncation energy $E_{\rm max}$ = 12.5 MeV, are unable to reproduce the data. The full calculation provides a breakup cross section in fair agreement with experiment. With identical conditions of the calculations, the model therefore provides a consistent description of elastic scattering and of breakup cross sections.

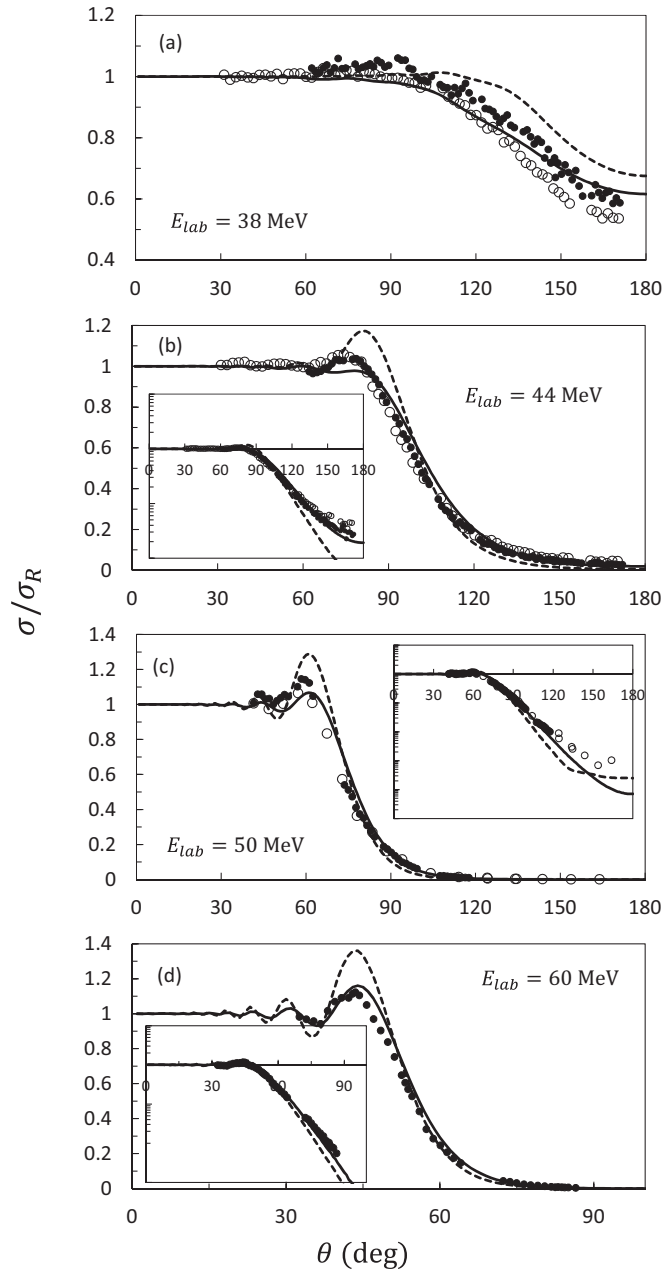

FIG. 7. ^{9}Be + ^{208}Pb elastic cross sections (divided by the Rutherford cross section) at different ^{9}Be laboratory energies. Dashed lines: single-channel calculations limited to the ^{9}Be ground state; solid lines: full calculations. The insets show the cross sections on a logarithmic scale. The experimental data are taken from Ref. [11] (filled circles) and Ref. [48] (open circles).

D. ^{9}Be + ^{208}Pb fusion

With the present model, we also address the calculation of the fusion cross sections. At energies below the Coulomb barrier, the fusion cross section has been shown to be strongly overestimated by theory [22]. In Ref. [22], the authors use a simple ^{8}Be + n two-body model of ^{9}Be, and they conclude that the coupling to the breakup channels leads to a strong enhancement of the total fusion cross section as compared

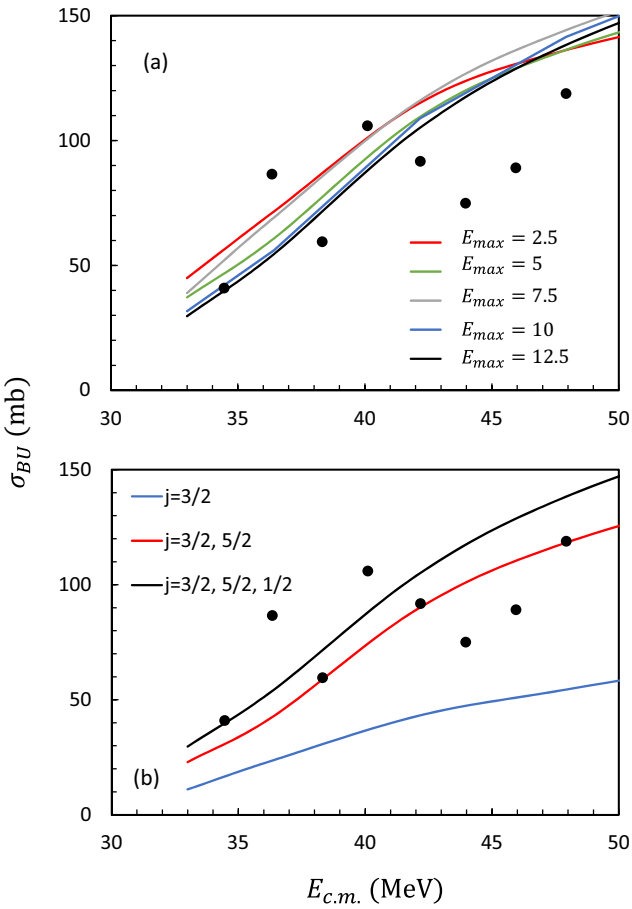

FIG. 8. (Color online) ^{9}Be + ^{208}Pb breakup cross section (25) as a function of the truncation energy $E_{\max}$ (upper panel) and of the ^{9}Be partial waves j (lower panel). The experimental data (filled circles) are taken from Ref. [13].

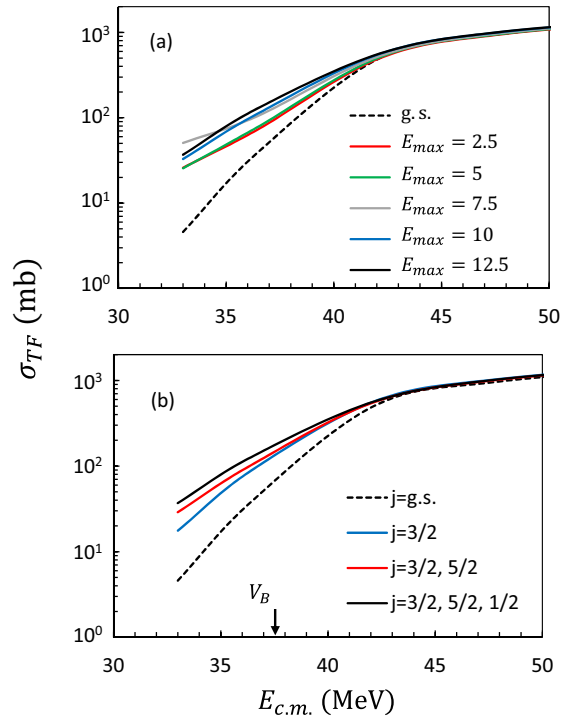

FIG. 9. (Color online) Total fusion cross sections σ_{TF} for different truncation energies $E_{\max}$ (in MeV, upper panel), and numbers of ^{9}Be partial waves (lower panel). The Coulomb barrier energy V_B is indicated by a vertical arrow.

to the data at sub-barrier energies. They investigate several ^{9}Be-target systems, but they do not consider elastic scattering.

In the present work, the description of ^{9}Be + ^{208}Pb fusion is improved in two ways: more realistic $\alpha + \alpha + n$ wave functions are used for ^{9}Be, and identical conditions (optical potentials and discretization of the continuum) are used for all processes. This unified and consistent treatment significantly enhances the reliability of the model, since no parameter is fitted, and since the theory can be tested on well-known elastic-scattering data.

The total fusion cross section essentially involves two contributions: that of complete fusion, where the whole projectile is absorbed, and that of incomplete fusion, where only a part of the projectile charge is absorbed by the target. As far as total fusion is concerned, the cross section can be obtained by using the scattering matrices [see Eqs. (26) and (27)]. The CDCC total fusion cross sections obtained in this way are shown in Fig. 9, where we analyze the convergence against the truncation energy (upper panel) and against the ^{9}Be partial waves (lower panel). The Coulomb barrier is located at 37.6 MeV and is indicated by a vertical arrow. Above $E_{\rm cm} \approx 40$ MeV, the fusion cross sections are weakly sensitive to the breakup channels. Calculations limited to the ^{9}Be ground state (dashed lines) provide a very realistic approximation. Below 40 MeV, however, breakup channels lead to a strong enhancement of the total fusion cross section. This is partly associated with the reduction of the breakup cross section (see Fig. 8) when the truncation energy increases. Again, convergence is reached for rather large $E_{\max}$ values.

Above the Coulomb barrier, the present calculation overestimates the data by about a factor of 2. Results provided by Eqs. (26) and (27) are presented in Fig. 10 as red lines. This overestimation is due to the different definitions adopted for fusion in the experiment and in the calculation. That is, the theory, Eq. (27), defines fusion as the absorption of the whole projectile or any of its fragments, including the neutron. On the other hand, the experimental cross section only includes contributions from the absorption of charge [15]. Thus, the two cross sections differ by the neutron absorption, which, owing to the lack of a Coulomb barrier, may be quite large. The CDCC calculation can be adapted to the experimental conditions by using the equivalent definition (32) of the fusion cross section. Of course, when the three components of the potential are included in (32), Eqs. (27) and (32) should provide identical cross sections. This comparison represents a strong test of the calculation, since both methods are numerically rather different.

With Eq. (32), we can simulate the experimental conditions, by removing the imaginary part of the $n - ^{208}$Pb potential. The results obtained in this way are shown in Fig. 10 as black lines. By excluding the neutron capture, we obtain excellent agreement with experiment above $E_{\rm cm} \approx 40$ MeV. This is

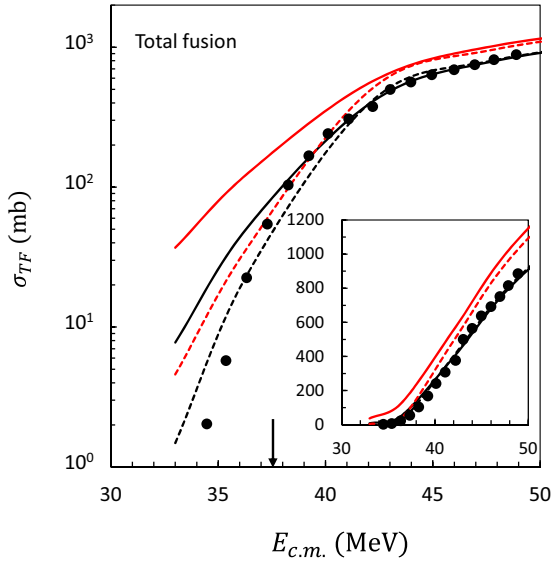

FIG. 10. (Color online) Total fusion cross sections with (black lines) and without (red lines) removal of the neutron capture. The dashed lines represent the single-channel calculations, and the solid lines represent the full calculations. The Coulomb barrier energy V_B is indicated by a vertical arrow.

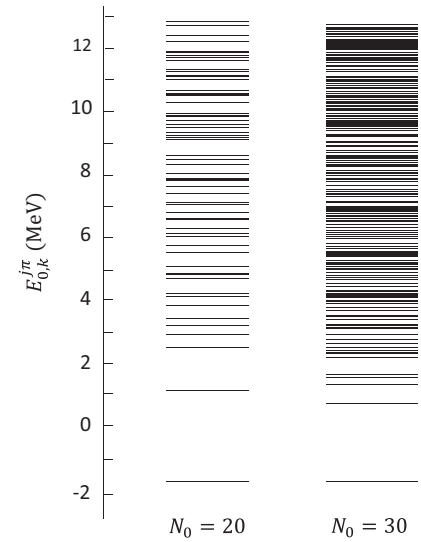

FIG. 11. ^{9}Be pseudostates with different numbers of basis functions: $N_0 = 20$ (left) and $N_0 = 30$ (right). Energies are defined from the $\alpha + \alpha + n$ threshold.

more clearly shown in the inset, drawn on a linear scale. We confirm previous CDCC calculations [22,49], in which the influence of breakup channels was shown to increase at sub-barrier energies. Below the Coulomb barrier, the single-channel calculation is in better agreement with experiment, and the full calculation overestimates the data. This discrepancy is common to most CDCC fusion calculations (see, for example, Fig. 1 of Ref. [22]), and it deserves further investigation.

E. Numerical issues

In this section we briefly discuss the sensitivity of the various cross sections against the continuum discretization and against the α-^{208}Pb potential. These tests allow us to assess the accuracy that may be expected from four-body CDCC calculations. In both cases, we compare calculations limited to $j = 3/2^-$ and $E_{\max} = 12.5$ MeV, to keep acceptable computer times. As we are essentially interested in qualitative aspects, it is reasonable to assume that the conclusions would be similar when all j values are included.

Let us first discuss the discretized continuum, which can be modified by changing the number of Lagrange basis functions, N_0. In all calculations until now, $N_0 = 20$ has been used. Using larger values of course improves the precision of the discretized continuum but strongly increases computer times. An additional calculation has been performed with $N_0 = 30$ (limited to $j = 3/2^-$, but the truncation energy $E_{\max}$ is identical). The continuum spectrum is shown in Fig. 11 and is compared to the conditions used throughout the paper. The number of continuum levels is 63 for $N_0 = 20$ and 235 for $N_0 = 30$; i.e., the level density is increased by a factor of 4.

The ratios

$$R_{N_0} = \frac{\sigma(N_0 = 30)}{\sigma(N_0 = 20)} \tag{32}$$

are shown in Fig. 12 for elastic scattering ($\theta = 60^\circ$ and 90°), for breakup, and for fusion. Although the level density is much higher for $N_0 = 30$, elastic scattering is virtually insensitive to the N_0 value. The breakup and fusion cross sections are more sensitive at low energies (6% and 8% at most). At these low energies, however, the cross sections (see Figs. 8 and 10) are quite low, and a variation of a few percent hardly affects the absolute values at the scale of the figures.

A similar sensitivity test is performed in Fig. 13, with the α-^{208}Pb optical potential. The two potentials essentially differ by their imaginary component. Goldring *et al.* [44], whose potential is adopted throughout the text, use a volume term. Here we perform calculations with the potential of Barnett and

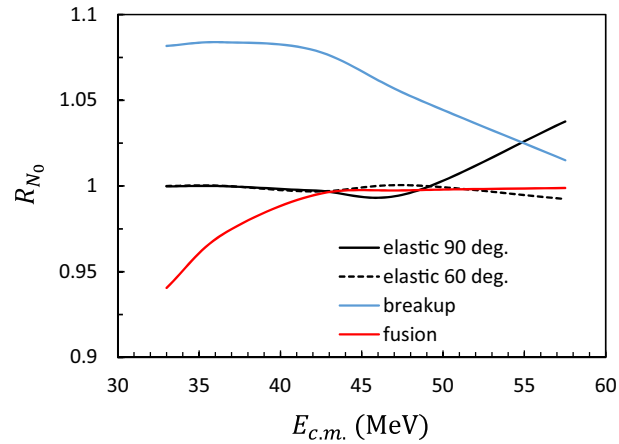

FIG. 12. (Color online) Ratios R_{N_0} [see Eq. (32)] for elastic scattering, breakup, and fusion.

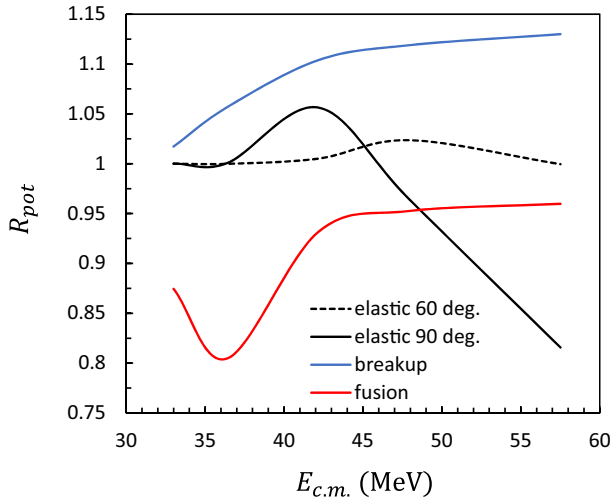

FIG. 13. (Color online) Ratios $R_{\rm pot}$ [see Eq. (33)] for elastic scattering, breakup, and fusion.

Lilley [50], which fits the α-^{208}Pb scattering with a surface term. Figure 13 displays the ratios

$$R_{\rm pot} = \frac{\sigma({\rm BL})}{\sigma({\rm GSM})}, \tag{33}$$

where BL and GSM stand for Refs. [50] and [44], respectively. The most visible effect is on the breakup cross section at high energies, where the difference reaches 12%. However, this sensitivity is much lower than the experimental uncertainties, and the choice of the potential does not affect the conclusions.

V. CONCLUSION

We have applied the four-body CDCC formalism to the ^{9}Be + ^{208}Pb system. In a first step, we have computed ^{9}Be wave functions within a three-body $\alpha + \alpha + n$ hyperspherical model. These calculations were performed for low-lying states but also for pseudostates, which represent positive-energy approximations of the continuum. The main advantage of the hyperspherical approach is that it treats the three-body continuum without any approximation concerning possible ^{8}Be + n or ^{5}He + α cluster structures, which actually are equivalent.

The three-body model of ^{9}Be relies on $\alpha + \alpha$ and $\alpha + n$ (real) interactions, which reproduce very well the elastic phase shifts. With these bare interactions, the ^{9}Be ground state is slightly too bound. We therefore introduce a phenomenological three-body force to reproduce the experimental ground-state energy. The spectroscopy of low-lying states is in fair agreement with experiment. When we express the wave functions in terms of ^{8}Be + n configurations, we confirm a strong component in the ^{8}Be(2^+) + n channel. This is particularly true for the $5/2^-$ excited state, which is almost pure ^{8}Be(2^+) + n, in agreement with experiment [14].

We used the ^{9}Be wave functions in a simultaneous calculation of ^{9}Be + ^{208}Pb elastic scattering, breakup, and fusion at energies close to the Coulomb barrier. CDCC calculations involving three-body projectiles require large computer times, owing to the level density. Until now, these calculations were limited to core + n + n projectiles [9,10,40], where a more limited number of partial waves were included. For ^{9}Be we have considered states with angular momentum $j^\pi = 1/2^\pm$, $3/2^\pm$, and $5/2^\pm$, with a large truncation energy. These conditions lead to heavy numerical calculations, in particular for fusion, but are necessary to achieve good accuracy of the cross sections. The use of the R matrix [43] is well adapted to large-scale calculations and can be optimized by using propagation techniques [51]. As expected, including continuum channels significantly improves the elastic cross sections.

With the CDCC method, breakup cross sections can also be derived. With a full basis, the CDCC cross sections are in good agreement with the data. We presented an exploratory study of ^{9}Be + ^{208}Pb fusion, with conditions of calculations identical to those of elastic scattering and breakup. We showed that fair agreement can be obtained simultaneously for the three processes. For fusion, however, the low-energy cross section is overestimated, owing to a strong influence of breakup channels. This result confirms previous works, performed in a simpler two-body model for the projectile. In the future, the same model could be used to analyze complete and incomplete fusion separately. A better understanding of the low-energy fusion data also deserves further studies.

We have assessed the sensitivity with respect to the $\alpha + \alpha + n$ continuum and to the choice of the α-^{208}Pb optical potential. This sensitivity is in general lower than the experimental uncertainties. As breakup is the most sensitive process, this issue will need to be treated carefully when high-precision breakup data become available.

ACKNOWLEDGMENTS

This text presents research results of the IAP programme P7/12 initiated by the Belgian-state Federal Services for Scientific, Technical and Cultural Affairs. PD is Directeur de Recherches of F.R.S.-FNRS, Belgium. Partial support from the Brazilian funding agencies CNPq, FAPESP, and FAPERJ is also acknowledged. MSH acknowledges support from the CAPES (ITA) Senior Visiting Professor Fellowship Program.

[1] N. Keeley, N. Alamanos, K. Kemper, and K. Rusek, Prog. Part. Nucl. Phys. **63**, 396 (2009).
[2] M. V. Zhukov, B. V. Danilin, D. V. Fedorov, J. M. Bang, I. J. Thompson, and J. S. Vaagen, Phys. Rep. **231**, 151 (1993).
[3] I. J. Thompson, B. V. Danilin, V. D. Efros, M. V. Zhukov, and J. S. Vaagen, J. Phys. G **24**, 1505 (1998).
[4] M. Theeten, D. Baye, and P. Descouvemont, Phys. Rev. C **74**, 044304 (2006).

[5] P. Descouvemont, C. Daniel, and D. Baye, Phys. Rev. C **67**, 044309 (2003).
[6] G. H. Rawitscher, Phys. Rev. C **9**, 2210 (1974).
[7] M. Yahiro, Y. Iseri, H. Kameyama, M. Kamimura, and M. Kawai, Prog. Theor. Phys. Suppl. **89**, 32 (1986).
[8] M. Yahiro, T. Matsumoto, K. Minomo, T. Sumi, and S. Watanabe, Prog. Theor. Phys. Suppl. **196**, 87 (2012).
[9] T. Matsumoto, E. Hiyama, K. Ogata, Y. Iseri, M. Kamimura, S. Chiba, and M. Yahiro, Phys. Rev. C **70**, 061601 (2004).
[10] M. Cubero *et al.*, Phys. Rev. Lett. **109**, 262701 (2012).
[11] R. J. Woolliscroft, B. R. Fulton, R. L. Cowin, M. Dasgupta, D. J. Hinde, C. R. Morton, and A. C. Berriman, Phys. Rev. C **69**, 044612 (2004).
[12] S. K. Pandit *et al.*, Phys. Rev. C **84**, 031601 (2011).
[13] R. J. Woolliscroft, N. M. Clarke, B. R. Fulton, R. L. Cowin, M. Dasgupta, D. J. Hinde, C. R. Morton, and A. C. Berriman, Phys. Rev. C **68**, 014611 (2003).
[14] T. A. D. Brown *et al.*, Phys. Rev. C **76**, 054605 (2007).
[15] M. Dasgupta *et al.*, Phys. Rev. Lett. **82**, 1395 (1999).
[16] M. Dasgupta *et al.*, Phys. Rev. C **70**, 024606 (2004).
[17] N. Keeley, K. W. Kemper, and K. Rusek, Phys. Rev. C **64**, 031602 (2001).
[18] V. V. Parkar, V. Jha, S. K. Pandit, S. Santra, and S. Kailas, Phys. Rev. C **87**, 034602 (2013).
[19] A. Diaz-Torres and I. J. Thompson, Phys. Rev. C **65**, 024606 (2002).
[20] L. F. Canto, P. R. S. Gomes, R. Donangelo, and M. S. Hussein, Phys. Rep. **424**, 1 (2006).
[21] K. Hagino and N. Takigawa, Prog. Theor. Phys. **128**, 1001 (2012).
[22] V. Jha, V. V. Parkar, and S. Kailas, Phys. Rev. C **89**, 034605 (2014).
[23] J. Raynal and J. Revai, Nuovo Cim. A **68**, 612 (1970).
[24] C. D. Lin, Phys. Rep. **257**, 1 (1995).
[25] D. Baye, Phys. Stat. Sol. **243**, 1095 (2006).
[26] P. Descouvemont, Eur. Phys. J. A **12**, 413 (2001).
[27] K. Arai, P. Descouvemont, D. Baye, and W. N. Catford, Phys. Rev. C **68**, 014310 (2003).
[28] K. Arai, Y. Ogawa, Y. Suzuki, and K. Varga, Phys. Rev. C **54**, 132 (1996).
[29] V. Voronchev, V. Kukulin, V. Pomerantsev, and G. Ryzhikh, Few-Body Syst. **18**, 191 (1995).
[30] R. Álvarez-Rodríguez, A. S. Jensen, E. Garrido, and D. V. Fedorov, Phys. Rev. C **82**, 034001 (2010).
[31] J. Casal, M. Rodríguez-Gallardo, J. M. Arias, and I. J. Thompson, Phys. Rev. C **90**, 044304 (2014).
[32] B. R. Fulton *et al.*, Phys. Rev. C **70**, 047602 (2004).
[33] B. Buck, H. Friedrich, and C. Wheatley, Nucl. Phys. A **275**, 246 (1977).
[34] H. Kanada, T. Kaneko, S. Nagata, and M. Nomoto, Prog. Theor. Phys. **61**, 1327 (1979).
[35] D. Baye, Phys. Rev. Lett. **58**, 2738 (1987).
[36] I. J. Thompson, B. V. Danilin, V. D. Efros, J. S. Vaagen, J. M. Bang, and M. V. Zhukov, Phys. Rev. C **61**, 024318 (2000).
[37] I. Tanihata, H. Hamagaki, O. Hashimoto, Y. Shida, N. Yoshikawa, K. Sugimoto, O. Yamakawa, T. Kobayashi, and N. Takahashi, Phys. Rev. Lett. **55**, 2676 (1985).
[38] D. R. Tilley, J. H. Kelley, J. L. Godwin, D. J. Millener, J. E. Purcell, C. G. Sheu, and H. R. Weller, Nucl. Phys. A **745**, 155 (2004).
[39] P. Descouvemont, Nucl. Phys. A **699**, 463 (2002).
[40] M. Rodríguez-Gallardo, J. M. Arias, J. Gómez-Camacho, R. C. Johnson, A. M. Moro, I. J. Thompson, and J. A. Tostevin, Phys. Rev. C **77**, 064609 (2008).
[41] I. J. Thompson, F. M. Nunes, and B. V. Danilin, Comput. Phys. Commun. **161**, 87 (2004).
[42] L. F. Canto and M. S. Hussein, *Scattering Theory of Molecules, Atoms and Nuclei* (World Scientific, Singapore, 2013).
[43] P. Descouvemont and D. Baye, Rep. Prog. Phys. **73**, 036301 (2010).
[44] G. Goldring, M. Samuel, B. A. Watson, M. C. Bertin, and S. L. Tabor, Phys. Lett. B **32**, 465 (1970).
[45] A. J. Koning and J. P. Delaroche, Nucl. Phys. A **713**, 231 (2003).
[46] T. Druet and P. Descouvemont, Eur. Phys. J. A **48**, 147 (2012).
[47] A. Di Pietro *et al.*, Phys. Rev. C **85**, 054607 (2012).
[48] N. Yu, H. Q. Zhang, H. M. Jia, S. T. Zhang, M. Ruan, F. Yang, Z. D. Wu, X. X. Xu, and C. L. Bai, J. Phys. G **37**, 075108 (2010).
[49] A. Diaz-Torres, I. J. Thompson, and C. Beck, Phys. Rev. C **68**, 044607 (2003).
[50] A. R. Barnett and J. S. Lilley, Phys. Rev. C **9**, 2010 (1974).
[51] T. Druet, D. Baye, P. Descouvemont, and J.-M. Sparenberg, Nucl. Phys. A **845**, 88 (2010).